

Crystal structure and monoclinic distortion of glaserite-type $\text{Ba}_3\text{MnSi}_2\text{O}_8$

Maxim Avdeev^{1,2*}, Qingbo Xia^{1,2}, Matthew Sale^{1,2}, Morgan Allison², Chris D. Ling^{1,2}

¹ *Australian Nuclear Science and Technology Organisation, New Illawarra Road, Lucas Heights NSW 2234, Australia*

² *School of Chemistry, The University of Sydney, Sydney 2006, Australia*

Abstract

Crystal structure and magnetic properties of glaserite-type $\text{Ba}_3\text{MnSi}_2\text{O}_8$ were investigated using variable temperature neutron powder diffraction and magnetometry. At room temperature the composition is hexagonal and the crystal structure is best described by the P-3m1 space group ($a \sim 5.7 \text{ \AA}$, $c \sim 7.3 \text{ \AA}$) with the apical oxygen atom modelled on a split site. On cooling below $\sim 250 \text{ K}$ the structure undergoes a phase transition into a monoclinic C2/c form ($\sqrt{3}a_{\text{hex}}$, a_{hex} , $2c_{\text{hex}}$, $\beta \sim 90^\circ$). Analysing diffraction data in terms of symmetry-adapted distortion modes suggests that the transition is primarily driven by increasing in-plane displacements of O1, which in turn results in the coupled tilting of $[\text{SiO}_4]$ and $[\text{MnO}_6]$ octahedra and in-plane displacements of Ba1 atoms. Magnetic susceptibility measurements and neutron powder diffraction data show no evidence for long-range magnetic ordering down to 1.6 K, although the development of magnetic diffuse scattering suggests that a magnetic transition may take place at lower temperature.

1. Introduction

Light emitting diodes (LED) are steadily replacing incandescent light sources owing to their higher energy efficiency and longer lifetime. A large family of silicates with the general formula $\text{A}_3\text{MSi}_2\text{O}_8$ ($\text{A}=\text{Ca}, \text{Sr}, \text{Ba}$; $\text{M}=\text{Mg}$) has attracted substantial interest as phosphor materials for LEDs.^{1, 2} In particular, glaserite-type hexagonal $\text{Ba}_3\text{MgSi}_2\text{O}_8$ shows very high tunability of emission which depends on the type of activation ion (Eu^{2+} , Mn^{2+} , Tb^{3+}) or mixture thereof^{3, 4}. The incorporation of Mn^{2+} into the structure was assumed to occur on the Mg^{2+} site due to its similar ionic radius; however, the end member $\text{Ba}_3\text{MnSi}_2\text{O}_8$ was never investigated in detail. Although synthesis of $\text{Ba}_3\text{MnSi}_2\text{O}_8$ has been reported before, only the symmetry and unit cell dimensions were presented based on X-ray powder diffraction (XRPD) data.⁵ The hexagonal symmetry and unit cell dimensions for $\text{Ba}_3\text{MnSi}_2\text{O}_8$ were reported to be very similar to those of $\text{Ba}_3\text{MgSi}_2\text{O}_8$ but the proposed space group was different: P6/mmm (#191),⁵ rather than P-3m1(#164)⁶⁻⁸ or P-3(#147)^{9, 10}. The lack of detailed crystal structural information motivated us to undertake a detailed crystal structural investigation of $\text{Ba}_3\text{MnSi}_2\text{O}_8$. Since the P-3 and P-3m1 models proposed for presumably isostructural $\text{Ba}_3\text{MgSi}_2\text{O}_8$ differ only subtly in the arrangement of oxygen atoms, we used neutron powder diffraction (NPD) which allows us to more accurately locate them in the presence of heavy elements than is

possible with XRPD. In order to separate the dynamic and static oxygen disorder, discussed further in detail herein, NPD data were collected at low temperature. They revealed a structural phase transition, which we investigated further by variable temperature NPD. Additionally, the magnetic properties were probed by magnetometry and low-temperature NPD.

2. Experimental

The powder sample of $\text{Ba}_3\text{MnSi}_2\text{O}_8$ was prepared by a solid state reaction using BaCO_3 (99.98%, Aldrich), MnCO_3 (>98.0%, B.D.H.) and SiO_2 (99.98%, Aldrich) as starting materials. The stoichiometric reactants were well mixed by ball milling with acetone at 360 rpm for 2h. After drying at 80°C, the homogeneously milled mixture was sintered at 800 °C for 10h to decompose the carbonates, following with an intermediate grinding. The final product $\text{Ba}_3\text{MnSi}_2\text{O}_8$ was obtained by undergoing a sintering process at 1200 °C for 20h.

Progress of the synthesis was monitored by collecting XRPD data on Panalytical X'Pert Pro diffractometer. Sintering was repeated until XRPD data of the sample did not change between successive treatments. The XRPD pattern for the final product agreed very well with the data reported for $\text{Ba}_3\text{MnSi}_2\text{O}_8$ in the original paper⁵ and showed presence of Ba_2SiO_4 , a very common by-product in synthesis of similar silicates, e.g., $\text{Ba}_3\text{MgSi}_2\text{O}_8$.⁶ In the case of $\text{Ba}_3\text{MnSi}_2\text{O}_8$, formation of Ba_2SiO_4 also results from minute oxidation of Mn^{+2} into Mn_3O_4 , which was found in the sample at the 1.4(1) wt% level.

Neutron powder diffraction (NPD) data were collected on the high-resolution powder diffractometer ECHIDNA at the OPAL research reactor (ANSTO, Lucas Heights, Australia). The sample was loaded in powder form into a cylindrical vanadium can and NPD data were collected using a neutron wavelength of 1.6215 Å or 2.4395 Å in the temperature range from 1.6 K to 450 K. The Loopstra-Laar-Rietveld analysis^{11, 12} was performed using the GSAS suite of programs¹³ with the EXPGUI front-end¹⁴, and Fullprof¹⁵. Crystal structure and difference Fourier maps were visualized using the VESTA program.¹⁶

The temperature-dependent magnetization of the samples was measured using a Quantum Design Physical Properties Measurement System (PPMS) with a vibrating sample magnetometer (VSM) probe from 2 to 300 K in an applied magnetic field 1 kOe, under zero field-cooled (ZFC) and field-cooled (FC) conditions.

3. Results and discussion

3.1. Room temperature neutron powder diffraction. Hexagonal structure.

The glaserite crystal structure type has a general formula $\text{XY}_2[\text{M}(\text{TO}_4)_2]$ and is illustrated in Fig. 1. The structure can be viewed as one built of $\frac{2}{\infty}[\text{M}(\text{TO}_4)_2]$ layers interleaved with X and Y cations. In the case of

Ba₃MnSi₂O₈ X=Y=Ba and Ba1 and Ba2 atoms occupy two inequivalent sites 1b(0,0,1/2) and 2d(1/3,2/3,z), respectively (Fig. 1). Oxygen atoms of two types, O1 and O2, occupy two inequivalent sites 2d(1/3,2/3,z) and 6i(x,-x,z) coordinating Si with the ratio 1:3. The three equatorial O2 oxygen atoms of the silicate groups connect the three adjacent [MnO₆] octahedra, while apical O1 atoms point to the interlayer space filled with Ba atoms. As the result, the O1 and O2 atoms are coordinated by Si⁺⁴+Ba1⁺² and Si⁺⁴+Mn⁺², respectively. O1 may be expected to be more labile due to longer and weaker Ba1-O1 bond, compared to Mn-O2. This is discussed in further detail below on the basis of our NPD results.

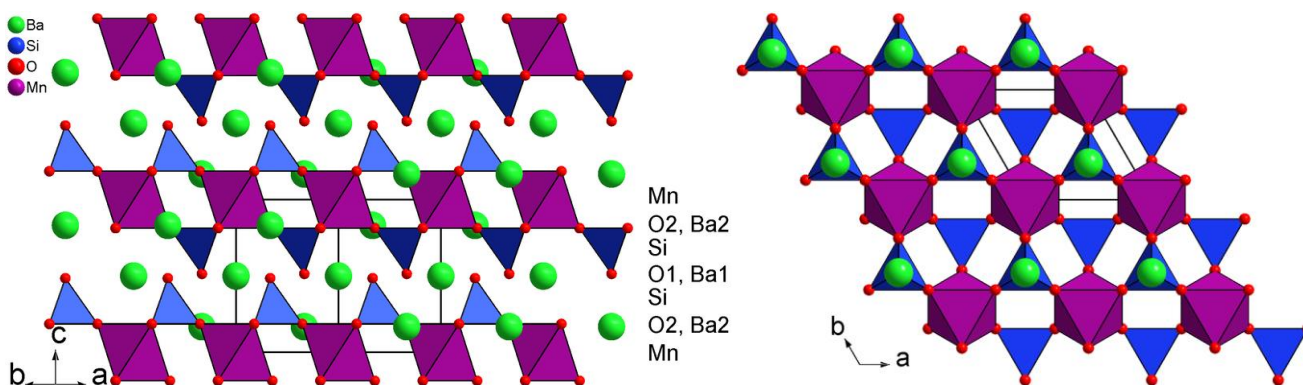


Figure 1. Hexagonal structure of glaserite-type Ba₃MnSi₂O₈ along (110) (left) and (001) (right). Solid black lines outline the hexagonal unit cell with $a \sim 5.7$ Å, $c \sim 7.3$ Å.

The Loopstra-Laar-Rietveld analysis^{11, 12} of the NPD data collected at room temperature revealed that a hexagonal model with space group P-3m1 (#146) and $a \sim 5.7$ Å, $c \sim 7.3$ Å indexed all the diffraction peaks of the main phase, yielding acceptable agreement with the experimental data. However, examination of the obtained structural parameters revealed that apical Si-O1 distance is noticeably shorter than equatorial Si-O2, and the isotropic displacement parameter of O1 is anomalously large - about three times higher than that of O2 (Model 1 in Table 1). Difference Fourier maps also clearly showed additional off-axis nuclear density (Model 1 in Table 2). The same observation was previously made for other hexagonal glaserite-type materials and ascribed to librational movement of tetrahedral groups, e.g., K₃Na(SeO₄)₂^{17, 18}, K₃Na(MoO₄)₂¹⁹, K₃Na(RuO₄)₂ and Rb₃Na(RuO₄)₂²⁰.

The anomalously high isotropic thermal parameter of O1 and short Si-O1 distance were also observed for Ba₃MgSi₂O₈. Several different crystal structural models were proposed to describe the apparent in-plane displacement of O1 from the ideal fixed ($x=1/3, y=2/3$) position. Aitasalo et al. proposed a model with O1 in a site of lower symmetry 6i(x,-x,z).⁶ Iwata et al. proposed a model in which not only the O1 site but also O2 and Ba1 are split.⁷ Based on NPD data, Park et al. proposed a superstructure described by the P-3 space group with oxygen displacements ordered in a ($\sqrt{3}a, \sqrt{3}a, c$) hexagonal supercell.⁹ All three models were tested against our NPD data for Ba₃MnSi₂O₈ (models 4-6 in Tables 1 and 2, respectively). In addition, we

tested the ideal glaserite model with isotropic displacement parameters (model 1), anisotropic displacement parameters for O1 only (model 2), and all atoms modelled anisotropically (model 3). Finally, we also tested a model describing [SiO₄] groups as rigid-body units in combination with the Translation-Libration-Screw (TLS) formalism²¹ which has previously been successfully applied to polyanionic materials such as silicates²² (model 7).

The results for the tested seven models are summarized in Tables 1 and 2. When comparing the models, attention was paid not only to the R-factors indicating quality of the NPD data fit, but also to the residual nuclear scattering density in difference Fourier maps. From comparison of the tested models, several conclusions can be drawn.

Modelling O1 anisotropically (model 2) significantly improves agreement between the calculated and experimental NPD data. The fit quality is practically identical to that for the model with a split O1 site⁶ using the same number of variables, cf. models 2 and 4 in Table 1. The resulting axially oblate ellipsoid of atomic displacements for O1 in model 2 also substantially reduces the residual nuclear scattering density in the unit cell compared to that for the isotropic model 1, although not as well as the model with a split O1 site: cf. values for models 1, 2 and 4 in Table 2.

Splitting of the O2 and Ba1 sites in addition to O1, following Iwata et al.⁷, results in further improvement (model 5 in Tables 1 and 2) but not as significant as modelling all atoms in the ideal glaserite anisotropically (model 3).

In contrast to Ba₃MgSi₂O₈,⁹ our NPD data for Ba₃MnSi₂O₈ showed no evidence of supercell reflections. As the results, refinement using the ($\sqrt{3}a, \sqrt{3}a, c$) P-3 model of Park et al. produced improvements neither in R-factors nor residual density of the difference Fourier map, despite the substantially higher number of variables (Table 1 and 2).

Finally, model 7 with coupled translational and librational movement of the rigid [SiO₄] group (with the four Si-O distances fixed to the value most commonly observed in silicates²³) gave an inferior fit (Table 1 and 2). This suggests that the [SiO₄] groups in Ba₃MnSi₂O₈, and most likely other glaserite-type materials, are not truly rigid bodies, the apical O1 oxygen atoms are more labile than O2, which results in local silicate group distortion.

Comparison of the seven models tested for Ba₃MnSi₂O₈ showed that the fully anisotropic model #3 produced the best agreement with our room temperature NPD data (Table 1). This is in agreement with the bulk of literature on crystal structure determination for glaserite-type oxides. However, we emphasize that such a model is clearly only an approximation as it cannot resolve the problem of the unphysically short Si-O1 distance. The natural step was to combine the split O1 model #4 with the fully anisotropic description of all the other atoms. Indeed, model #8 yielded not only the same refinement quality but also the lowest residual nuclear density (Tables 1 and 2). We therefore conclude that this is the most adequate model of

crystal structure of $\text{Ba}_3\text{MnSi}_2\text{O}_8$ and likely all the other hexagonal glaserite-type oxides in the hexagonal form. This was further confirmed in the detailed study of $\text{Ba}_3\text{MnSi}_2\text{O}_8$ at low temperature, as described below. The final refinement plot and refined crystal structural parameters for $\text{Ba}_3\text{MnSi}_2\text{O}_8$ at room temperature are presented in Figure 2 and Table 3, respectively.

In order to investigate whether the local disorder of O1 atoms is static or dynamic, we further collected low temperature NPD data which revealed that on cooling, $\text{Ba}_3\text{MnSi}_2\text{O}_8$ undergoes a structural phase transition.

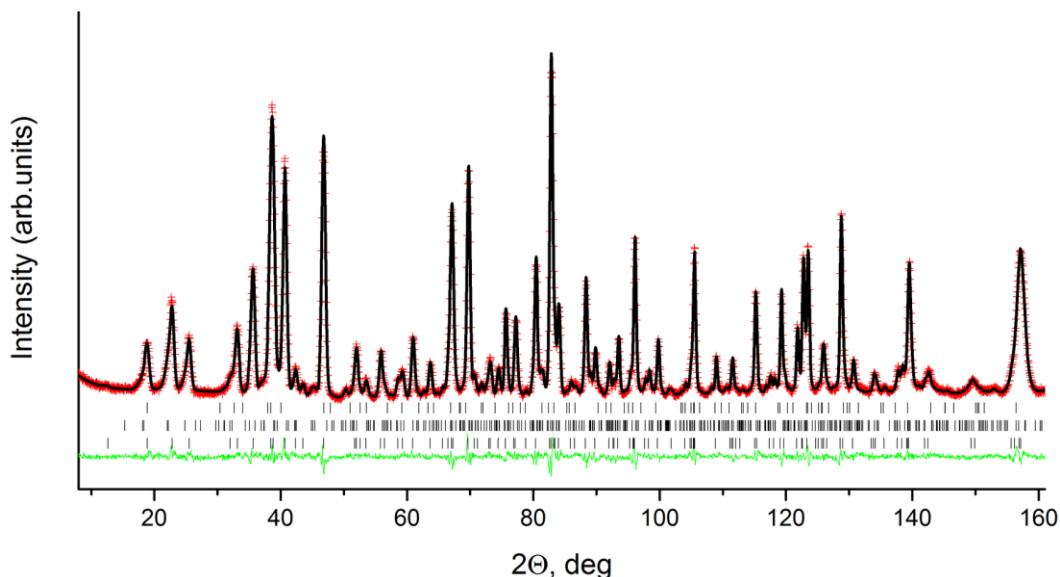


Figure 2. Room temperature NPD data fit ($\lambda=1.6215 \text{ \AA}$). Red crosses, black and green solid lines are experimental and calculated data and their difference, respectively. The tick marks from top to bottom show peak positions for $\text{Ba}_3\text{MnSi}_2\text{O}_8$, Ba_2SiO_4 , and Mn_3O_4 , respectively.

3.2. Low-temperature neutron powder diffraction data. Monoclinic structure.

The NPD data collected at 3 K clearly showed peak splitting indicative of symmetry lowering from the parent hexagonal cell. Structural distortions of glaserite-type are well known and unsurprising, as corner sharing of octahedra and tetrahedra in the ${}^2_{\infty}[\text{M}(\text{SiO}_4)_2]$ layers (Figure 1) allows great flexibility of the structure in response to atom size mismatch, cooling, or applied pressure, similarly to other corner sharing structure types, such as perovskites.

In general, reports on symmetry lowering for the glaserite type agree that the hexagonal structure undergoes a monoclinic distortion. However, at least four different monoclinic structures have been reported. These include $(\sqrt{3}a_{\text{hex}}, a_{\text{hex}}, c_{\text{hex}})$ C2/m (e.g. $\text{CsK}_2\text{Ho}(\text{PO}_4)_2$ ²⁴), $(\sqrt{3}a_{\text{hex}}, a_{\text{hex}}, 2c_{\text{hex}})$ C2/c (e.g. $\text{Na}_2\text{BaCu}(\text{VO}_4)_2$ ²⁵), $(\sqrt{3}a_{\text{hex}}, a_{\text{hex}}, 2c_{\text{hex}})$ C2 (e.g. $\text{Sr}_3\text{Mg}(\text{SiO}_4)_2$ ¹⁰), and $(\sqrt{3}a_{\text{hex}}, a_{\text{hex}}, 2c_{\text{hex}})$ P2₁/c (e.g. merwinite $\text{Ca}_3\text{Mg}(\text{SiO}_4)_2$ ²⁶).

The corresponding models adapted for Ba₃MnSi₂O₈ were tested against the NPD data collected at 3 K. The results are summarized in Table 4. It is clear that the C2/c model provides a more adequate fit to the experimental data than C2/m. However, further symmetry lowering and consequent increase in the number of variables for the C2 and P2₁/c merwinite models by 28 and 29, respectively, provides only a slight improvement which is not statistically significant²⁷. Therefore, we can conclude that at low temperature, Ba₃MnSi₂O₈ is monoclinic and is best described by the C2/c space group and ($\sqrt{3}a_{\text{hex}}$, a_{hex} , $2c_{\text{hex}}$) unit cell. The final refinement plot and refined crystal structural parameters for Ba₃MnSi₂O₈ at 3 K are presented in Figure 3 and Table 5, respectively.

Comparison of the apical and three equatorial Si-O distances in the monoclinic form at 3 K (1.612(3) Å, 1.628(4) Å, 1.636(4) Å, and 1.665(5), respectively) to those in the hexagonal form at room temperature (1.600(3) Å and $3 \times 1.646(1)$ Å, respectively) suggests that the monoclinic-hexagonal phase transition is driven mainly by oxygen displacements. The additional degrees of freedom of the monoclinic structure allow both to increase the distance to the apical oxygen atom and reduce the distortion of the [SiO₄] tetrahedra overall. The distortion index for [SiO₄] defined as $1/4 \sum |(Si-O)_i - (Si-O)_{\text{ave}}| / (Si-O)_{\text{ave}}$ ²⁸ decreases from 0.0103 to 0.0093 at room temperature and 3 K, respectively.

In order to further investigate the mechanism of the monoclinic-hexagonal phase transition, we collected variable temperature NPD data in the range 3-300 K.

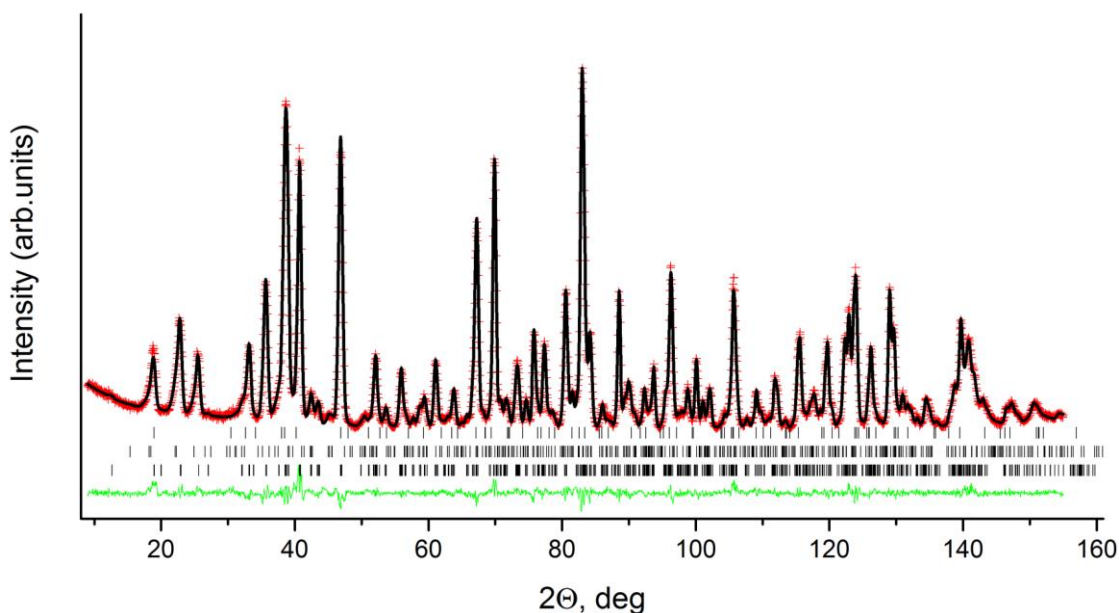


Figure 3. Low temperature 3 K NPD data fit ($\lambda=1.6215$ Å). Red crosses, black and green solid lines are experimental and calculated data and their difference, respectively. The tick marks from top to bottom show peak positions for Ba₃MnSi₂O₈, Ba₂SiO₄, and Mn₃O₄, respectively.

3.3. Variable temperature neutron powder diffraction data. Monoclinic-hexagonal phase transition.

Neutron powder diffraction data collected between 3 K and 280 K with 20 K steps revealed that the characteristic monoclinic peak splitting and additional weak peaks gradually reduce and then disappear around 240 K (Figure 4).

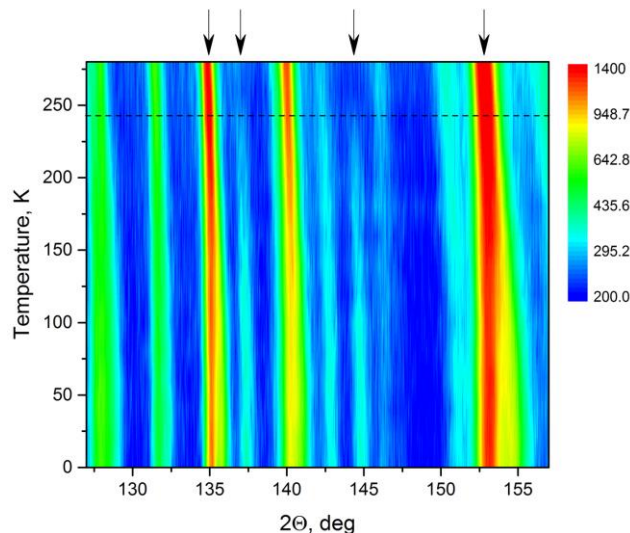


Figure 4. Neutron powder diffraction data as a function of temperature ($\lambda=2.4395 \text{ \AA}$). Intensity corresponds to pseudo color as indicated by the scale. Arrows highlight the characteristic peaks with monoclinic splitting and new peaks appearing below $\sim 240 \text{ K}$.

The subtlety of the monoclinic-hexagonal phase transition is illustrated in Figure 5, which shows both the room temperature hexagonal structure transformed to the monoclinic setting by the $((2,1,0)(0,1,0)(0,0,2))$ matrix and the monoclinic structure at 3 K. Clearly, the transition is of displacive type with only slight tilting of $[\text{MnO}_6]$ octahedra and $[\text{SiO}_4]$ tetrahedra and shear of the $\frac{2}{\infty}[\text{M}(\text{TO}_4)_2]$ layers. This results in a monoclinic angle $\beta \sim 90.2^\circ$, which is very close to the ideal value of 90° .

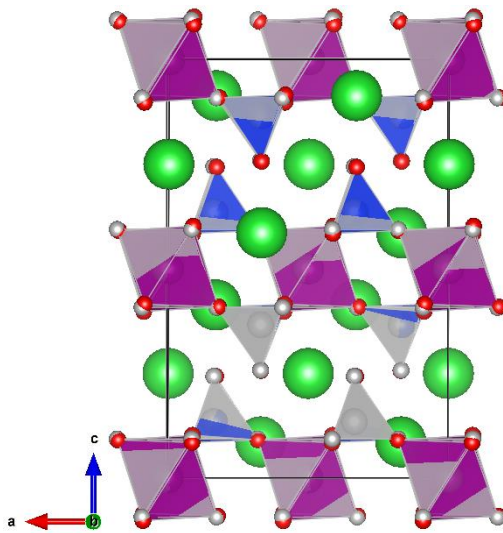


Figure 5. Room-temperature hexagonal structure of $\text{Ba}_3\text{MnSi}_2\text{O}_8$ overlapped with its monoclinic modification at 3 K (grey and colored, respectively) showing slight tilting of $[\text{MnO}_6]$ and $[\text{SiO}_4]$ and shear of the ${}^2_{\infty}[\text{M}(\text{TO}_4)_2]$ layers.

Analysis of crystal structure distortion in terms of symmetry-adapted distortion modes is a very illuminating way to understand driving forces behind a displacive phase transition. We performed such analysis with the ISODISTORT Software Suite²⁹ taking the room temperature and 3 K models (Tables 3 and 5) as high- and low-symmetry structures, respectively. The four distortion modes associated with the transformation of $\text{Ba}_3\text{MnSi}_2\text{O}_8$ from $P\text{-}3m1$ into $C2/c$, i.e., $\text{GM1}+$, $\text{GM3}+$, $\text{A2}+$, and $\text{A3}+$, are illustrated in Figure 6 and briefly described in Table 6. As can be seen from the values in Table 6, the $\text{A3}+$ mode (tilting of $[\text{MnO}_6]$ and $[\text{SiO}_4]$ around the a_{mon} -axis coupled with Ba1 displacement) has by far the largest amplitude and is clearly the primary distortion mode. It is followed by the $\text{GM3}+$ mode (tilting of $[\text{MnO}_6]$ and $[\text{SiO}_4]$ around b_{mon} -axis), while the $\text{GM1}+$ (axial stretching of $[\text{MnO}_6]$ along c_{mon} -axis) and $\text{A2}+$ (rotation of $[\text{SiO}_4]$ around c_{mon} -axis) modes have practically zero amplitudes. Examination of the individual atomic displacements from the corresponding positions in the room-temperature parent hexagonal structure revealed that the O1 atoms experience the largest shift by $\sim 0.25 \text{ \AA}$, followed by Ba1 ($\sim 0.16 \text{ \AA}$) and O2 which splits into three inequivalent sites (0.15, 0.13, 0.05). Ba2 and Si show negligible displacements and Mn remains in the fixed (0,0,0) position. The fact that O1 undergoes the largest displacement is not surprising in the light of the discussion in section 3.1. above.

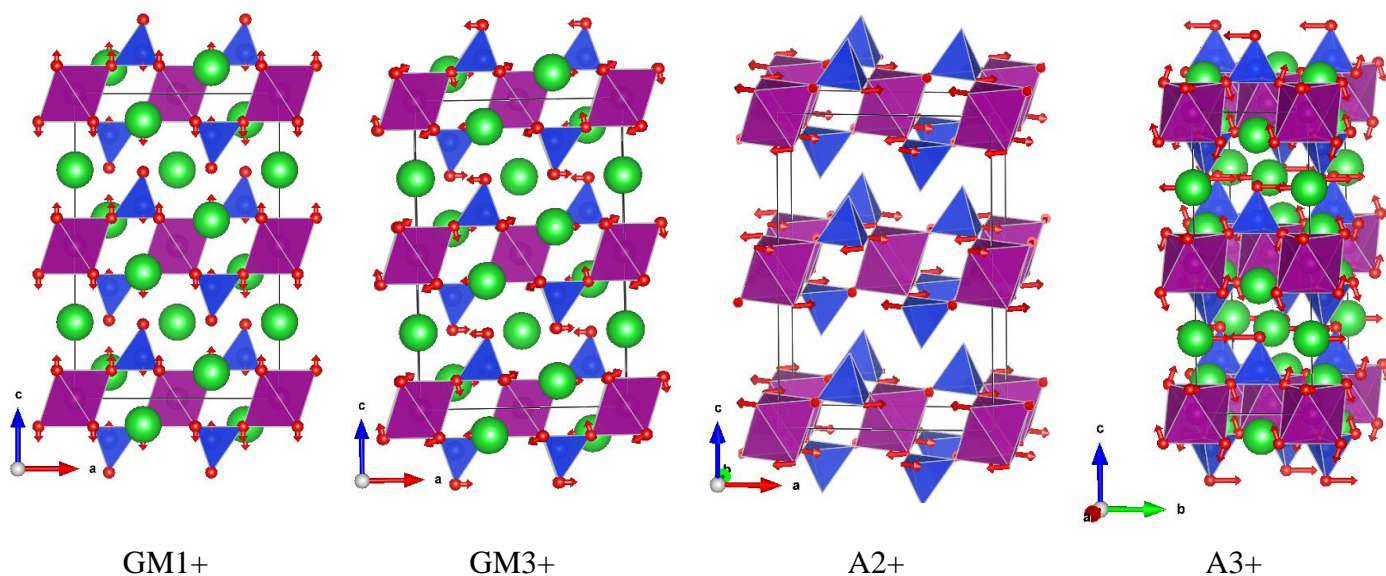


Figure 6. Distortion modes for the transition from P-3m1 to C2/c for Ba₃MnSi₂O₈. The arrow lengths are proportional to the mode amplitudes at 3 K but for clarity multiplied by factors of 10, 2, 15, and 0.5 for GM1+, GM3+, A2+, and A3+, respectively.

Once the crystal structural model in terms of symmetry-adapted distortion modes was established, the NPD data collected in the range from 3 K to 280 K were analysed in the same fashion in a sequential mode. Since the GM1+ and A2+ modes were found to be inactive (Table 6) their amplitudes were kept at zero, which reduced the number of distortion mode related variables from 19 to 13.

The obtained evolution of the unit cell parameters with temperature clearly indicated that the monoclinic distortion gradually decreases on heating from 3 K and the lattice becomes metrically hexagonal between 240 K and 260 K (Figure 7).

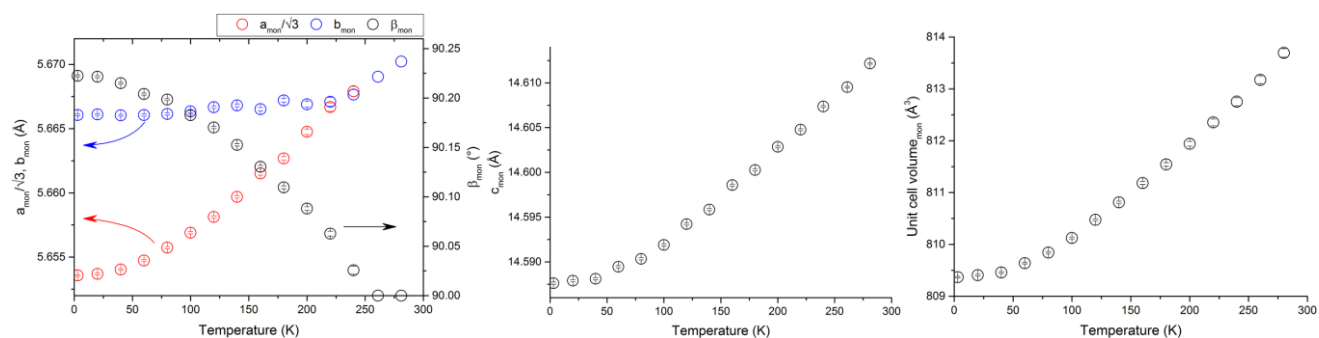


Figure 7. Monoclinic unit cell parameters $a_{\text{mon}}/\sqrt{3}$, b_{mon} , β_{mon} (left), c_{mon} (middle), and volume (right) as a function of temperature based on NPD data.

The temperature evolution of polarisation vector amplitudes for individual atoms is presented in Figure 8. Most of the values cluster around zero and only four, emphasized by thick solid lines, clearly stand out: displacement of O1 along the a_{mon} and b_{mon} axes (GM3+(O1) and A3+(O1), respectively); displacement of O2 along the c_{mon} axis (A3+(O2)); and displacement of Ba1 along the b_{mon} axis (A3+(Ba1)). The displacements of O2 and Ba1 gradually approach zero, similarly to all the other displacements. However, the behaviour of the O1 displacements associated with the GM3+ and A3+ modes is very peculiar - instead of vanishing, they approximately equalize and stabilize at around 0.3 in the temperature region of the hexagonal structure (Figure 8).

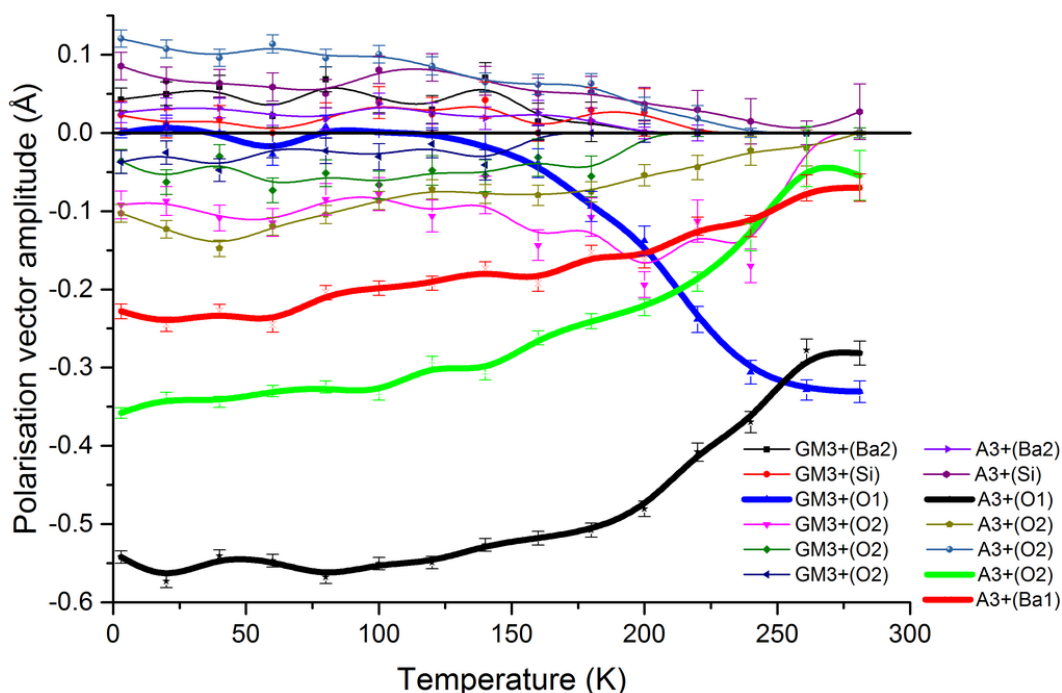


Figure 8. Polarisation vector amplitudes for individual atoms as a function of temperature based on NPD data. The amplitudes resulting in the largest displacements are emphasized as thick solid lines.

This behaviour can be easily understood if we consider the combined effect of the GM3+ and A3+ modes on the O1 atoms. The approximately equal polarisation vector amplitudes produce displacements of O1 toward one of the three nearest $[\text{MnO}_6]$ octahedra (Figure 9, left), which coincides with the direction of the residual nuclear density observed in the difference Fourier maps obtained for the isotropic hexagonal model #1 (Figure 9, right). Although in the monoclinic phase the GM3+ and A3+ modes produce only one particular displacement for each O1, we should bear in mind that at 260 K and above, the unit cell is metrically hexagonal. This is true even when the structure is refined as monoclinic, i.e., $a_{\text{mon}}/\sqrt{3}=b_{\text{mon}}\sim 5.67\text{\AA}$ (Figure 7, left), which results in three indistinguishable displacements that can be described as a three-fold split of the O1 site in the hexagonal form (model #8 in Table 1).

Alternatively, the argument can be reversed and we can say that the driving force of the monoclinic phase transition is the increasing displacement of O1 away from the hexagonal $2d(1/3,2/3,z)$ site, which eventually causes shearing of the ${}^2_{\infty}[\text{M}(\text{TO}_4)_2]$ layers and loss of the three-fold symmetry.

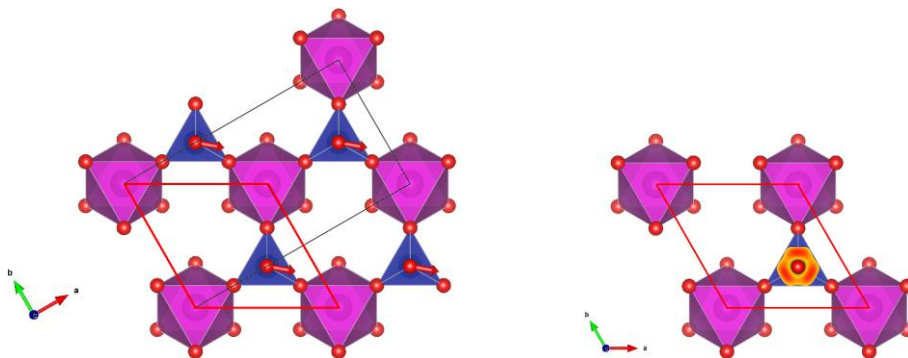


Figure 9. Left: displacement of O1 atoms in the monoclinic model due to the combined effect of the GM3+ and A3+ modes of approximately equal amplitudes, as determined at 280 K. Right: residual nuclear density in the vicinity of O1 in the hexagonal model #1 (Table 1). Thick red line shows the parent hexagonal unit cell in both phase modifications.

Finally, we note that the evolution of both cell parameters (Figure 7) and distortion mode amplitudes (Figure 8) suggest second-order character of the phase transition. Although two phase transitions were observed for some glaserite-type compounds, with possible intermediate structures $P-3c1$ ($a_{\text{hex}}, a_{\text{hex}}, 2c_{\text{hex}}$) or $C2/m$ ($\sqrt{3}a_{\text{hex}}, a_{\text{hex}}, c_{\text{hex}}, \beta \sim 90^\circ$),^{18, 19, 30, 31} $\text{Ba}_3\text{MnSi}_2\text{O}_8$ appears to undergo a single phase transition via the two-dimensional irreducible representation A3+, which allows a continuous $P-3m1-C2/c$ transformation. That is also consistent with A3+ being the primary distortion mode associated with the in-plane displacement of apical O1 atoms, as discussed above. A less likely scenario is the pathway $P-3m1 \xrightarrow{\text{GM3+, 1st order}} C2/m \xrightarrow{\text{A2+, 2nd order}} C2/c$ with the $C2/m$ phase existing in a too narrow temperature range to have been observed in this study.

3.4. Magnetic properties of $\text{Ba}_3\text{MnSi}_2\text{O}_8$

Given that paramagnetic $d^5 \text{Mn}^{2+}$ ions are present in $\text{Ba}_3\text{MnSi}_2\text{O}_8$, a question arises as to whether the compound orders magnetically at low temperature. The magnetic susceptibility data presented in Figure S1 showed only one anomaly around 42 K, a well-known signature of the ferrimagnetic transition in Mn_3O_4 which is present in the sample at the level of $\sim 1.4\text{wt.}\%$ as discussed earlier. No other magnetic transitions are observed down to the lowest accessible temperature of 2 K. A fit to the Curie-Weiss law using the data in the temperature range 250-300 K yielded a negative Weiss temperature Θ_{CW} , indicating predominantly

antiferromagnetic interactions and an effective magnetic moment of $5.97 \mu_B$ (consistent with the expected spin-only value of $5.92 \mu_B$ for $d^5 \text{Mn}^{+2}$). Additional NPD data collected at 1.6 K also showed no evidence of long-range magnetic ordering, although comparison of the 1.6 K and 3 K NPD data sets revealed magnetic diffuse scattering developing in the former (Figure S2), which suggests a possible magnetic transition at lower temperature. The magnetic behaviour of $\text{Ba}_3\text{MnSi}_2\text{O}_8$ appears to be very similar to that of another Mn-based glaserite-type compound, $\text{Na}_2\text{BaMnV}_2\text{O}_8$, which also demonstrated a negative Weiss temperature and presumably a magnetic phase transition (observed in specific heat measurements).³²

4. Conclusions

The crystal structure of glaserite-type $\text{Ba}_3\text{MnSi}_2\text{O}_8$ was studied between 1.6 K and 300 K using neutron powder diffraction. In contrast to the original report on the synthesis of this oxide, the crystal structure at room temperature is described by the P-3m1 space group. On cooling below ~ 250 K, the material undergoes a slight monoclinic distortion and is best described by the C2/c space group. Detailed analysis of atomic displacements decomposed using symmetry-adapted distortion modes suggests that the transition is driven by increasing amplitude of the in-plane apical oxygen atom displacements, which are also present in the hexagonal structure in the form of local disorder. Magnetometry and low-temperature neutron powder diffraction data suggest that $\text{Ba}_3\text{MnSi}_2\text{O}_8$ remains paramagnetic down to 1.6 K, although developing magnetic diffuse scattering and analogy with another Mn-based glaserite $\text{Na}_2\text{BaMnV}_2\text{O}_8$ suggest that long-range magnetic ordering is likely to occur at lower temperature.

References

1. J. S. Kim; P. Jeon; J. Choi; H. Park; S. Mho; G. Kim, *Appl. Phys. Lett.* **2004**, 84, (15), 2931-2933.
2. J. S. Kim; A. K. Kwon; Y. H. Park; J. C. Choi; H. L. Park; G. C. Kim, *J. Lumin.* **2007**, 122, 583-586.
3. Y. Umetsu; S. Okamoto; H. Yamamoto, *J. Electrochem. Soc.* **2008**, 155, (7), J193-J197.
4. A. Birkel; N. A. DeCino; C. Cozzan; A. A. Mikhailovsky; B.-C. Hong; R. Seshadri, *Solid State Sciences* **2015**, 48, 82-89.
5. I. Georgieva; I. Ivanov; O. Petrov, *Powder Diffr.* **1996**, 11, (1), 26-27.
6. T. Aitasalo; A. Hietikko; J. Holsa; M. Lastusaari; J. Niittykoski; T. Piispanen, *Z Kristallogr Suppl* **2007**, 26, 461-466.
7. T. Iwata; T. Horie; K. Fukuda, *Powder Diffr.* **2009**, 24, (3), 180-184.
8. Y. Yonesaki; T. Takeji; N. Kumada; N. Kinomura, *J. Solid State Chem.* **2009**, 182, (3), 547-554.
9. C.-H. Park; S.-T. Hong; D. A. Keszler, *J. Solid State Chem.* **2009**, 182, (3), 496-501.
10. Y. Yonezaki, *Powder Diffr.* **2015**, 30, (1), 40-51.
11. B. van Laar; H. Schenk, *Acta Crystallographica Section A: Foundations and Advances* **2018**, 74, (2), 88-92.
12. B. Loopstra; H. Rietveld, *Acta Crystallographica Section B: Structural Crystallography and Crystal Chemistry* **1969**, 25, (4), 787-791.
13. A. C. Larson; R. B. Von Dreele, *Los Alamos National Laboratory Report LAUR 86-748* **2004**.
14. B. H. Toby, *J. Appl. Crystallogr.* **2001**, 34, 210-213.
15. J. Rodríguez-Carvajal, *Physica B: Condensed Matter* **1993**, 192, (1-2), 55-69.
16. K. Momma; F. Izumi, *J. Appl. Crystallogr.* **2011**, 44, (6), 1272-1276.
17. J. Fabry; T. Breczewski; V. Petříček, *Acta Crystallogr. Sect. B: Struct. Sci.* **1993**, 49, (5), 826-832.
18. M. Kaczmarek; B. Mróz, *Phys. Rev. B* **1998**, 57, (21), 13589.
19. J. Fábry; V. Petricek; P. Vanek; I. Cisarova, *Acta Crystallogr. Sect. B: Struct. Sci.* **1997**, 53, (4), 596-603.
20. K. M. Mogare; W. Klein; E.-M. Peters; M. Jansen, *Solid state sciences* **2006**, 8, (5), 500-507.
21. V. Schomaker; K. Trueblood, *Acta Crystallographica Section B: Structural Crystallography and Crystal Chemistry* **1968**, 24, (1), 63-76.
22. M. G. Tucker; M. T. Dove; D. A. Keen, *J. Phys.: Condens. Matter* **2000**, 12, (26), L425.
23. W. H. Baur, *Acta Crystallographica Section B: Structural Crystallography and Crystal Chemistry* **1978**, 34, (6), 1751-1756.
24. V. A. Efremov; P. P. Melnikov; L. N. Komissarova, *Revue de chimie minérale* **1985**, 22, (5), 666-675.
25. M. Von Postel; H. Müller-Buschbaum, *Z. Anorg. Allg. Chem.* **1992**, 618, (12), 107-110.
26. P. B. Moore; T. Araki, *Am. Mineral.* **1972**, 57, 1355-1374.
27. W. Hamilton, *Acta Crystallogr.* **1965**, 18, (3), 502-510.
28. W. Baur, *Acta Crystallographica Section B* **1974**, 30, (5), 1195-1215.
29. H. T. Stokes; D. M. Hatch; B. J. Campbell ISOTROPY Software Suite. iso.byu.edu
30. T. Krajewski; P. Piskunowicz; B. Mroz, *physica status solidi (a)* **1993**, 135, (2), 557-564.
31. J. Díaz-Hernández; J. Manes; M. Tello; A. López-Echarri; T. Breczewski; I. Ruiz-Larrea, *Phys. Rev. B* **1996**, 53, (21), 14097.
32. G. Nakayama; S. Hara; H. Sato; Y. Narumi; H. Nojiri, *J. Phys.: Condens. Matter* **2013**, 25, (11), 116003.

Table 1. Data analysis R-factors, apical (Si-O1) and basal (Si-O2) interatomic distances, and equivalent atomic displacement parameters U_{eq} for O1 and O2 atoms for crystal structural models tested against room temperature NPD data. Bold font shows the model which both provides the best agreement with the NPD data and is physically plausible.

#	Model	Wyckoff sequence	Sp. gr.	Variables	$R_p, \%$	$R_{wp}, \%$	$R_{F2}, \%$	Si-O1, Å	Si-O2, Å	$U_{11}(O1), \times 100, \text{Å}^2$	$U_{33}(O1), \times 100, \text{Å}^2$	$U_{eq}(O1), \times 100, \text{Å}^2$	$U_{eq}(O2), \times 100, \text{Å}^2$
1	Ideal glaserite, U_{iso} (all atoms)	id3ba	P-3m1	42	3.31	4.22	5.62	1.583(3)	1.652(1)	-	-	3.16(4)	0.93(2)
2	Ideal glaserite, $U_{ij}(O1)$	id3ba	P-3m1	43	3.10	3.89	5.02	1.582(3)	1.651(1)	4.56(8)	0.73(10)	3.28(8)	1.02(2)
3	Ideal glaserite, U_{ij} (all atoms)	id3ba	P-3m1	50	2.83	3.55	3.68	1.590(3)	1.646(1)	4.48(7)	0.70(10)	3.22(8)	1.08(4)
4	Split O1, Ref ⁶	i2d2ba	P-3m1	43	3.11	3.90	4.91	1.598(3)	1.650(1)	-	-	1.18(8)	1.00(2)
5	Split O1, O2, Ba1 sites, Ref ⁷	i3hd2a	P-3m1	46	2.89	3.63	3.96	1.606(3)	1.626(6)/1.664(3)	-	-	1.19(8)	0.71(2)
6	$\sqrt{3}a \times \sqrt{3}a \times c$ supercell, Ref ⁹	g6d2ba	P-3	61	3.16	3.97	3.83	1.591(3)	1.648(11)/1.659(14)/ 1.645(12)	-	-	2.34(5)	1.01(6)/0.72(5)/ 1.08(6)
7	Rigid body [SiO ₄] + TLS	id3ba	P-3m1	41	4.19	5.69	7.55	1.626(-) ²³	=Si-O1	-	-	2.37(4)	1.13(2)
8	Split O1, U_{ij}(all other atoms)	i2d2ba	P-3m1	50	2.86	3.58	3.68	1.600(3)	1.646(1)			1.30(8)	1.07(4)

Table 2. 3D difference Fourier maps, their cross-sections at $z=1/2$, and lowest/highest residual nuclear density based on room temperature NPD data for the models listed in Table 1. The isosurface levels for 3D maps and the scale for cross-sections are identical to those of the Model #1, i.e. $2.5e-2 \text{ fm}/\text{\AA}^3$ and $-3.9/+4.3e-2 \text{ fm}/\text{\AA}^3$, respectively.

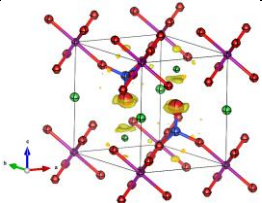
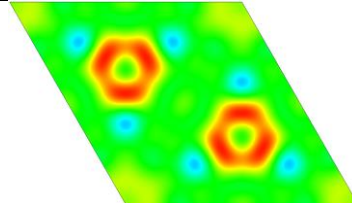
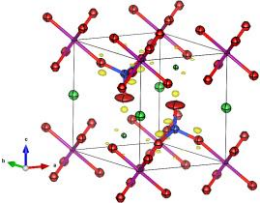
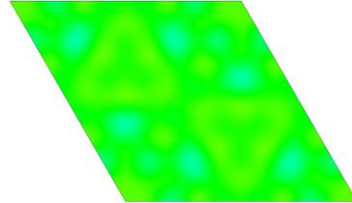
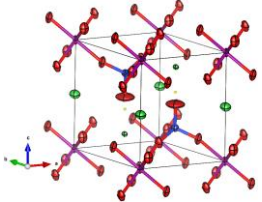
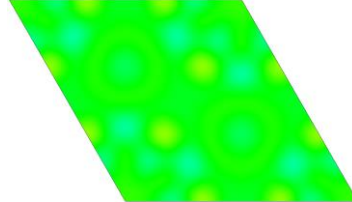
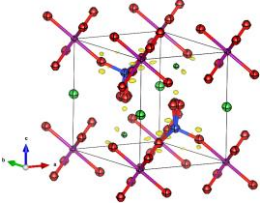
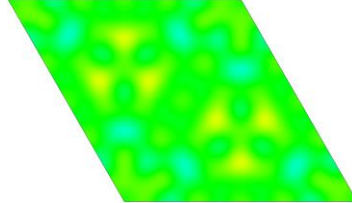
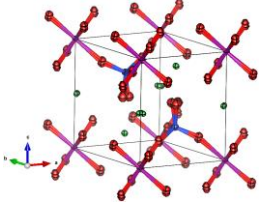
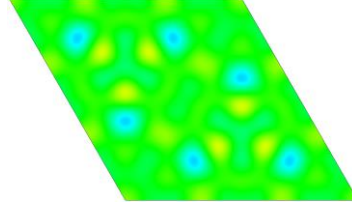
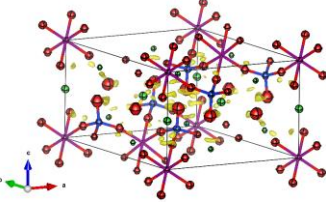
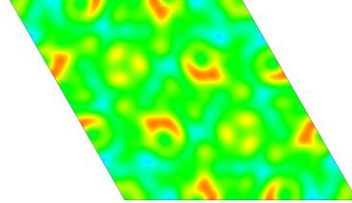
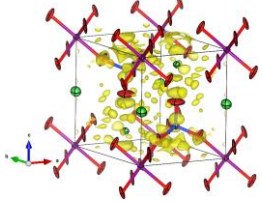
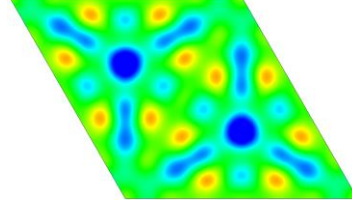
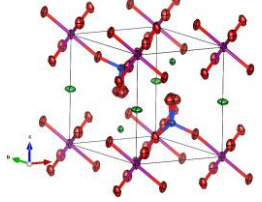
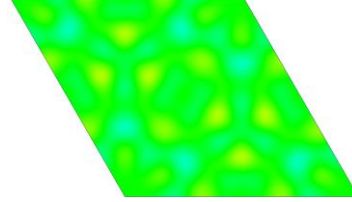
Model	Difference Fourier map	2D cross-section at $z=1/2$	min/max density, $\times 100 \text{ fm}/\text{\AA}^3$
1			-3.9/4.3
2			-3.8/3.6
3			-1.7/2.7
4			-3.3/3.1
5			-2.7/2.5
6			-3.5/3.9
7			-10.2/11.6
8			-1.9/2.3

Table 3. Refined crystal structural parameters for Ba₃MnSi₂O₈ based on room temperature neutron powder diffraction data. Space group P-3m1 (#164), a=5.67039(15) Å, c= 7.3062(2) Å.

Atom	x	y	z	U ₁₁ , Å ²	U ₂₂ , Å ²	U ₃₃ , Å ²	U ₁₂ , Å ²	U ₁₃ , Å ²	U ₂₃ , Å ²
Ba1	0	0	1/2	0.0142(8)	=U ₁₁	0.0097(18)	=U ₁₁ /2	-	-
Ba2	1/3	2/3	0.1719(3)	0.0038(5)	=U ₁₁	0.0031(9)	=U ₁₁ /2	-	-
Mn	0	0	0	0.0032(10)	=U ₁₁	0.0102(18)	=U ₁₁ /2	-	-
Si	1/3	2/3	0.7314(3)	0.0068(6)	=U ₁₁	0.0072(11)	=U ₁₁ /2	-	-
O1	1/3	2/3	0.5137(3)	0.0448(7)	=U ₁₁	0.0070(10)	=U ₁₁ /2	-	-
O2	0.17791(10)	=-x	0.81552(14)	0.0089(3)	=U ₁₁	0.0169(5)	0.0062(4)	0.0014(2)	=-U ₁₃

Table 4 Analysis summary for neutron powder diffraction data collected for Ba₃MnSi₂O₈ at 3 K. Bold font shows the best model.

#	Model	Wyckoff sequence	Sp. gr.	Variables	R _p , %	R _{wp} , %	R _{F2} , %	ICSD structure type or representative compound
1	C2/m ($\sqrt{3}a_{\text{hex}}, a_{\text{hex}}, c_{\text{hex}}, \beta \sim 90^\circ$)	ji4ca	C2/m	51	7.01	9.72	9.00	CsK ₂ Ho(PO ₄) ₂ ²⁴
2	C2/c ($\sqrt{3}a_{\text{hex}}, a_{\text{hex}}, 2c_{\text{hex}}, \beta \sim 90^\circ$)	id3ba	C2/c	60	2.85	3.61	2.38	Na₂BaCu(VO₄)₂²⁵
3	C2 ($\sqrt{3}a_{\text{hex}}, a_{\text{hex}}, 2c_{\text{hex}}, \beta \sim 90^\circ$)	c13ba	C2	88	2.71	3.48	1.88	Sr ₃ Mg(SiO ₄) ₂ ¹⁰
4	P2 ₁ /c ($\sqrt{3}a_{\text{hex}}, a_{\text{hex}}, 2c_{\text{hex}}, \beta \sim 90^\circ$)	e14	P2 ₁ /c	89	2.78	3.52	2.18	merwinite Ca ₃ Mg(SiO ₄) ₂ ²⁶

Table 5. Refined crystal structural parameters for Ba₃MnSi₂O₈ based on neutron powder diffraction data collected at 3 K. Space group C2/c (#15), a=9.7898(5) Å, b= 5.6654(3) Å, c=14.5851(8) Å, β=90.2278(12)°.

Atom	x	y	z	U _{iso} , Å ²
Ba1	0	0.0286(5)	0.25	0.0010(6)
Ba2	0.3316(4)	0.0049(5)	0.41385(13)	0.0011(4)
Mn	0	0	0	0.0020(7)
Si	0.33301(33)	0.0011(6)	0.13400(13)	0.0038(4)
O1	0.08581(35)	0.2766(6)	0.41531(19)	0.0035(5)
O2	0.33048(30)	-0.0445(4)	0.24304(12)	0.0063(5)
O3	0.17850(30)	0.0084(6)	0.0910(3)	0.0045(7)
O4	0.41215(30)	0.2398(5)	0.10198(14)	0.0016(5)

Table 6. Distortion modes for Ba₃MnSi₂O₈ and their amplitudes at 3 K with respect to the room temperature structure as a high-symmetry reference.

Mode	Description	Atoms involved	Amplitude at 3 K, Å
GM1+	Axial stretching and compression of [MnO ₆] octahedra and [SiO ₄] tetrahedra, respectively, and displacement of Ba2 and Si along c _{mon} -axis.	Ba2, Si, O1, O2	0.0199
GM3+	Coupled tilting of [MnO ₆] and [SiO ₄] around b _{mon} -axis and distortion of [SiO ₄]	Ba2, Si, O1, O2	0.1076
A2+	Coupled anti-phase rotation of [MnO ₆] and [SiO ₄] around c _{mon} -axis	O2	0.0193
A3+	Coupled tilting of [MnO ₆] and [SiO ₄] around a _{mon} -axis, distortion of [SiO ₄] and displacement of Ba1 along b _{mon} -axis	Ba1, Ba2, Si, O1, O2	0.6818